

The future of wind energy in California: Future projections with the Variable-Resolution CESM



Meina Wang ^{a, b, *}, Paul Ullrich ^{a, b}, Dev Millstein ^b

^a University of California, Davis, Davis, CA, USA

^b Lawrence Berkeley National Laboratory, Berkeley, CA, USA

ARTICLE INFO

Article history:

Received 28 October 2017

Received in revised form

22 March 2018

Accepted 9 April 2018

Available online 12 April 2018

Keywords:

Wind energy

Climate change

Variable-resolution climate modeling

California

ABSTRACT

Shifting wind patterns are an expected consequence of global climate change, with direct implications for wind energy production. However, wind is notoriously difficult to predict, and significant uncertainty remains in our understanding of climate change impacts on existing wind generation capacity. In this study, historical and future wind climatology and associated capacity factors at five wind turbine sites in California are examined. Historical (1980–2000) and mid-century (2030–2050) simulations were produced using the Variable-Resolution Community Earth System Model (VR-CESM) to understand how these wind generation sites are expected to be impacted by climate change. A high-resolution statistically downscaled WRF product provided by DNV GL, reanalysis datasets MERRA-2, CFSR, NARR, and observational data were used for model validation and comparison. These projections suggest that wind power generation capacity throughout the state is expected to increase during the summer, and decrease during fall and winter, based on significant changes at several wind farm sites. This study improves the characterization of uncertainty around the magnitude and variability in space and time of California's wind resources in the near future, and also enhances our understanding of the physical mechanisms related to the trends in wind resource variability.

Published by Elsevier Ltd.

1. Introduction

Renewable energy installations, particularly wind and solar, have been rapidly deployed in recent years in an effort to displace existing fossil fuel-based energy sources [1]. Within the U.S., California was the first state to undertake development of large wind farms starting in the early 1980s. In terms of absolute capacity, California's wind-generated electricity has roughly doubled during the past five years, to meet 6.81% of the states total system power (as of 2016). Research has also indicated that, globally, a moderate wind energy deployment plan in which wind displaces coal (i.e., 14% wind-derived electricity generation by 2050) would help delay by 1–6 years crossing the 2 °C warming threshold, often considered a lower threshold for dangerous climate change [2]. The growing adoption of wind power emphasizes that wind is a proven, reliable, and cost-effective source of low-emission power that can grow at scale. However, wind power is also dependent on sufficiently high wind speeds, which can significantly vary by location and time

period. Several past studies have demonstrated historical decreases in near-surface wind speeds over many regions of the Northern Hemisphere, including the United States [3,4]. Consequently, an understanding of present and future wind climatology is very important when determining where investments in the construction of new wind farms should be made. In particular, given that the lifespan of wind farms is typically around 20–25 years, climate change over the coming decades has the potential to significantly affect the wind farm productivity [5].

Like many other renewable energy technologies, wind energy is influenced by climate change through changes in global energy balance and resulting shifts in atmospheric circulation patterns [6]. The few studies that have examined the impact of climate change on wind resources over California using global and/or regional climate models [7] have been largely inconclusive. These prior studies have shown sensitivity to model setup, including choice of physics scheme, downscaling method, and number of models used [8–13]. Furthermore, the spatial variability of wind energy resources and its sensitivity to model settings emphasizes the benefit of higher resolution models and multiple model inter-comparisons [7].

* Corresponding author. University of California, Davis, Davis, CA, USA.

E-mail address: mnawang@ucdavis.edu (M. Wang).

In order to better understand how climate change will impact wind energy resources in California, this study has utilized a state-of-the-art global climate modeling system with support for regional refinement, the Variable-Resolution Community Earth System Model (VR-CESM). The goal of this study is twofold: First, to validate, analyze, and understand the biases in the historical hub-height wind field as produced by VR-CESM, and second to use VR-CESM to understand how climatological trends will impact wind power. Seasonal synoptic-scale patterns were investigated as part of this work to better understand how shifts in large-scale systems can impact local-scale changes in wind energy. For this study we have divided California into two primary sub-domains: Northern California (NC) sub-domain, which includes Shiloh and Altamont Pass sites, and Southern California (SC) sub-domain, which includes Alta, Tehachapi, San Gorgonio, and Ocotillo sites. These five wind farm locations constitutes a selection of both wind farm sites currently at service, and wind project sites are slated for new development. Note the Tehachapi wind farm ($35^{\circ}06'08''$ N $118^{\circ}16'58''$ W) is very close to the Alta Wind Energy Center ($35^{\circ}1'16''$ N $118^{\circ}19'14''$ W), so only the Alta site was used for assessing the wind field in that area. Fig. 1 depicts this region, along with the six wind farms and three atmospheric sounding locations.

Previous studies [14,15] utilizing VR-CESM have demonstrated its competitiveness in studying high-resolution regional climatology when compared to other regional climate models, especially when non-local processes have significant influence on the local climatology. VR-CESM has demonstrated a much better representation of climatology within regions of complex topography, due to the relatively fine regional resolution compared with conventional GCM simulations [16–18].

The remainder of the paper is as follows. Section 2 describes the VR-CESM model setup and the datasets used in this study. In section 3, historical wind speeds are compared across all datasets, including the available sounding observational sites and surface observations. Future projections from the mid-century VR-CESM

simulation are discussed in section 4. Changes to the synoptic-scale climatological background fields are also analyzed and described in this section. Discussion and conclusions follow in section 5.

2. Datasets

Two model simulations, three reanalysis products, and two observational datasets are used for model validation and inter-comparison of wind speed at hub height (summarized in Table 1). In this section we provide an overview of these products.

2.1. Summary of datasets

VR-CESM (Global climate model product.) CESM version 1.5.5, a fully coupled atmospheric, land, ocean, and sea ice model, was utilized for this study. All simulations used the F-component set (FAMIPIC5), which prescribes sea-surface temperatures and sea ice but dynamically evolves the atmosphere and land surface component models. The atmospheric component mode is the Community Atmosphere Model, version 5.3 (CAM5) [19] with the spectral-element (SE) dynamical core [20] in its variable-resolution (VR) configuration [21]. The VR model grid used for this study, depicted in Fig. 2, was generated for use in CAM and CLM with the open-source software package SQuadGen [22,23]. On this grid the finest horizontal resolution is 0.125° (~ 14 km), with a quasi-uniform 1° mesh over the remainder of the globe. Two simulations were conducted using this grid structure: First, the historical run covers the period from October 1st, 1979 to December 31st, 2000, with first three months discarded as the spin-up period, for a total of 21-years outputted every three hourly. This historical time period was chosen to provide an adequate sampling of the inter-annual variability, and to coincide with the time period from the rest of the modeling and reanalysis datasets. For projections of future wind energy change, our mid-century simulation ran with the “business as usual” Representative Concentration Pathway 8.5 (RCP8.5) [24]

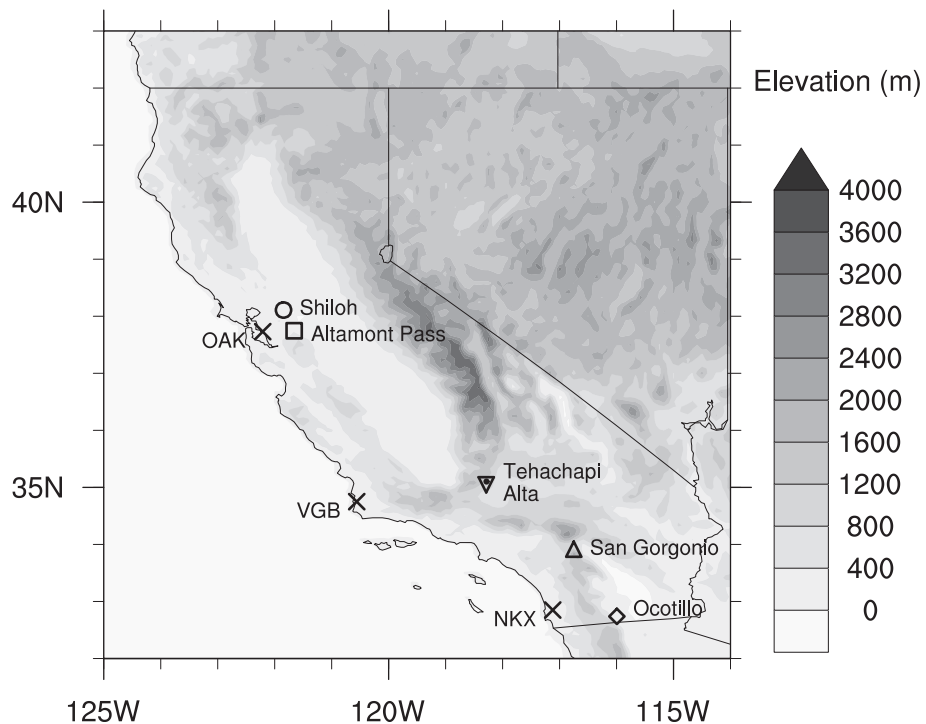


Fig. 1. Six wind farm sites, and three sounding locations assessed in this study. Markers shown for each location are consistent as in the rest of the figures.

Table 1

Model, reanalysis, and observational datasets used in this study.

Dataset	Spatial resolution	Temporal resolution	Time period
VR-CESM	~14 km (0.125°)	3-hourly	1980–2000; 2030–2050
Virtual Met	4 km	1-hourly	1980–2000
MERRA-2	~55 km (0.5°)	3-hourly	1980–2000
CFSR	~55 km (0.5°)	6-hourly	1980–2000
NARR	32 km	3-hourly	1980–2000
ISD	Point stations	1-hourly	1980–2000
Soundings	OAK, VGB NKK	12-hourly 12-hourly	1980–2000 1990–2000

from October 1st, 2029 to December 31st, 2050, again discarding the first three months for a total of 21-years. The future time period was chosen to emphasize the mid-century focus of this study and avoid divergence in the predicted impacts among different RCPs. Greenhouse gas (GHG) and aerosol forcings are prescribed based on historical or RCP8.5 concentrations for each simulation. More details on VR-CESM can be found in Ref. [14].

DNV GL Virtual Met (Dynamically-downscaled regional model product). The Det Norske Veritas Germanischer Lloyd (DNV GL) Virtual Met product is derived from a hybrid dynamical-statistical downscaling system based upon the Weather Research and Forecasting (WRF) model and an analog-based ensemble downscaling method (denoted as Virtual Met in Table 1). The predictor consists of a coarse resolution WRF simulation that is run for the entire simulation period. To provide training data for the statistical model, a nested version of the same model is run at high resolution. The period over which the coarse and high-resolution runs overlap is called the training period, while the remaining portion is termed downscaling period. To downscale the predictor data outside of the training period, the best matching coarse estimates (termed “analog”) over the training period are found. The downscaled solution is then constructed from the set of high-resolution values that correspond to the best matching coarse analogs. This method is based upon Delle Monache et al. [25,26].

The WRF simulation uses telescoping computational grids with one-way interaction. For this study the respective horizontal grid increments are 20 km and 4 km, with the 4 km grid centered over California. The initial and lateral boundary conditions are specified using MERRA-2, which is widely accepted in the wind energy community as a high-quality (albeit coarse resolution) wind product. The coarse model was run for the entire 01 Jan 1980–31

Dec 2015 period, and generated output every hourly, whereas the nested 4 km grid was run only during the last year of the full simulation (01 Jan 2015 to 31 Dec 2015). The high resolution downscaled dataset is then reconstructed for the entire 36-year period using the 4 km resolution training data and the 20 km simulation (both from the same WRF model configuration). The result is an hourly time series at each 4 km grid point for January 1st 1980 to December 31st 2015. Wind speed and direction at hub heights, including 50 m, 80 m, 140 m, are predicted and output. This study purely utilized the 80 m wind speed output, as the 80 m hub height is typical for most present-day industrial wind turbines. DNV GL served solely as a data provider for this project, and is not responsible for any results from this study.

MERRA-2 (Reanalysis product). The Modern-Era Retrospective analysis for Research and Applications, Version 2 (MERRA-2) is a reanalysis product for the satellite era using the Goddard Earth Observing System Data Assimilation System Version 5 (GEOS-5) produced by Global Modeling and Assimilation Office (GMAO) at NASA [27]. MERRA-2 integrates several improvements over the first version MERRA product, as described in Ref. [28]. For the fields used in this study, the spatial resolution is ~55 km with 3-hourly output frequency from 1980 to present. Vertical interpolation of MERRA-2 data, as described in the following section 3, was performed to calculate hub height wind speed at 80 m. Variables used in vertical interpolation were extracted from two subsets: 3-hourly instantaneous pressure level assimilation [29], and hourly instantaneous single level assimilation [30] (extracted at 3-hourly frequency).

CFSR (Reanalysis product). The Climate Forecast System Reanalysis (CFSR) from NCEP (National Centers for Environmental Prediction) is a global, coupled reanalysis that spans from 1979 to present, with ~55 km spatial resolution and 6-hourly temporal resolution of relevant wind fields [31]. Notably, this temporal resolution is the lowest out of the five dataset used. The analysis subset was used in this study, and vertical interpolation was performed at 6-hourly frequency.

NARR (Reanalysis product). The North American Regional Reanalysis (NARR), another NCEP reanalysis product, features a slightly higher spatial resolution of ~32 km. It is a dynamically-downscaled data product with spatial coverage over North America, with 3-hourly temporal resolution from 1979 through present [32]. Hub height wind speeds from NARR were also calculated at this frequency.

ISD (In-situ observations). The Integrated Surface Database (ISD) from NOAA's National Centers for Environmental Information (NCEI) were used for assessment of hourly 10 m wind speed from model and reanalysis. The ISD observational stations are distributed globally, with the highest concentration of stations found in North America. Stations across California that provide full year data were selected. As not all stations had continuous temporal coverage between 1980 and 2000, each year was examined separately so as to maximize the number of available stations. To compare 10 m wind speeds from model and reanalysis datasets to ISD, the nearest grid point values to each of the ISD stations was used. Coastal stations were neglected in the analysis of 10 m winds, due to coastal biases that tend to occur in near-surface coarse-resolution reanalysis. These biases tend to emerge because similarity theory is typically employed to extract 10 m wind speeds, which produces distinctly different results over the ocean and land surface.

Upper air soundings (In-situ observations). Upper air soundings (vertical wind profiles) from all the available locations across California are incorporated into the comparison (University of Wyoming, Department of Atmospheric Science <http://weather.uwyo.edu/upperair/sounding.html>). The three sounding locations used in this study are OAK at Oakland airport (station number 72493), VBG at Vandenberg Air Force Base (72393), and NKX at San

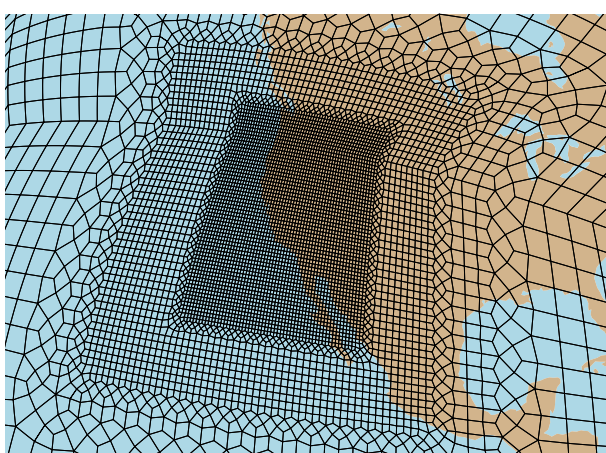


Fig. 2. The VR-CESM grid used in this study, constructed by first successively refining a cubed-sphere grid with a 1°(111 km) quasi-uniform resolution to a resolution of 0.125° (~14 km) over the western USA.

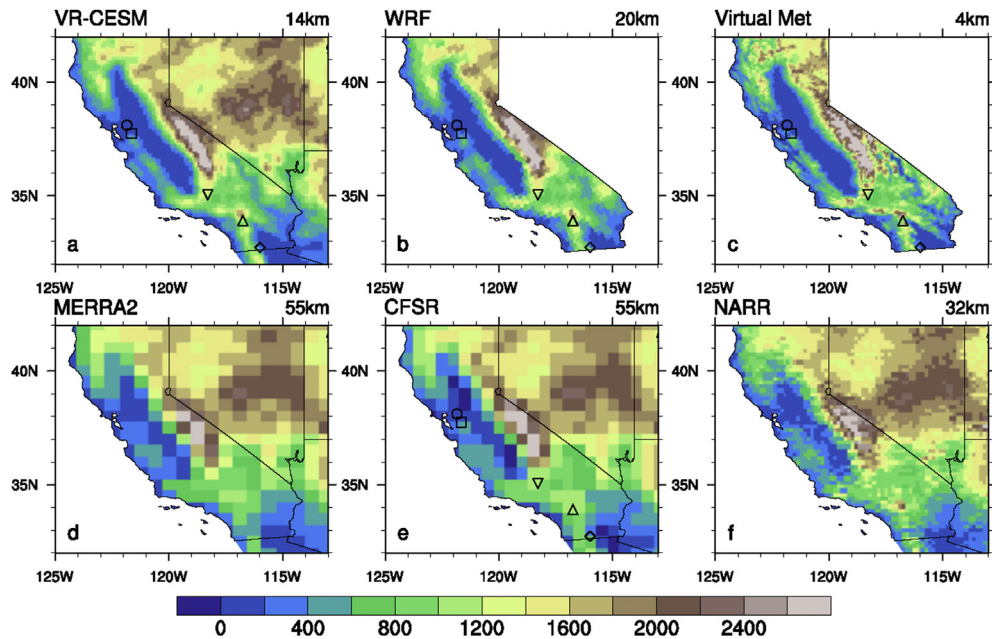


Fig. 3. Topographical representation of California and surrounding regions from model (top row) and reanalysis (bottom row) datasets.

Diego (72293) (see Fig. 1). The time period used in this study from the first two stations spans 1980 to 2000. NKX only has data available starting from September 1989, so only the full years 1990–2000 were assessed. Soundings were collected every 12 hourly at 00Z and 12Z, and logarithmic vertical interpolation was performed to calculate 80 m wind at each sounding location. However, this logarithmic interpolation from sparsely sampled profile data could introduce uncertainties into the calculation.

2.2. Representation of topography

Local topography is particularly important in representing the wind field, particularly in the regions of significant topographic variability that tend to be well-suited for wind power generation. Consequently, the importance of model resolution cannot be understated. Topographic profiles from each of the models and reanalysis datasets are plotted in Fig. 3. As can be seen here, DNV GL WRF model ran at 20 km resolution (b), which captures the dynamical wind field at this resolution, and then statistically downscaled to 4 km resolution (c). VR-CESM uses a relatively smooth topography by comparison, due to its slightly lower spatial resolution of 14 km (a). MERRA-2, CFSR, and NARR (d-f) all have much more poorly refined topography, with a poor representation of the coastal ranges that are important for shaping the wind field. Note that these differences also imply that each model has a different altitude for the wind farms and sounding stations used in this study.

3. Model comparison and wind resources characterization

3.1. Methodology

The wind speed at each wind farm location was determined using nearest grid point values to each wind farm site. To obtain 80 m wind vectors for this study, vertical interpolation was performed on 3-hourly VR-CESM, 3-hourly MERRA-2, 6-hourly CFSR, and 3-hourly NARR products from 1980 to 2000. As mentioned above, 80 m wind output is available directly from the DNV GL

Virtual Met data product used in this study, so values are extracted directly from the output from 1980 to 2000. Vertical interpolation of VR-CESM data uses the 3D wind field on hybrid surfaces and 10 m-altitude wind speed, which is computed from similarity theory. For VR-CESM data, the interpolation procedure is as follows: (1) the CAM5 hybrid coordinates are first converted to pressure coordinates within the column being analyzed, (2) the height of each pressure surface above ground level (AGL) is computed by subtracting the surface geopotential height from the geopotential height of the model level, (3) two model levels that bound the desired interpolation altitude are selected or, if the interpolation altitude is below the lowest model level, the lowest model level and 10 m wind speed field are used, and (4) logarithmic interpolation is applied to obtain the wind speed at the desired interpolation altitude. Specifically, the interpolation was performed by fitting a log equation with the two levels bounding the altitude to be calculated, then interpolating the wind at desired altitude [33]. Vertically interpolated wind speeds from MERRA-2, CFSR, NARR, and sounding observations were all obtained a similar procedure, and were calculated at three hub heights (50 m, 80 m, and 140 m). Further, wind speed at 80 m was logarithmically interpolated for all three sounding profile locations, and compared with interpolated 80 m wind speed at each sounding locations from all five model/reanalysis datasets.

The wind field enters into the maximum potential wind power $P(W)$ via the expression $P = \frac{1}{2} \rho A U^3$, where ρ is air density (kg/m^3), A is the cross section area of the turbine rotor (m^2), and U is wind speed at hub height (m/s). Given the cubic relationship between wind speed and wind energy potential, even a small change in wind speeds can lead to a substantial change to wind energy production. The energy contribution of wind turbines to the electric power system is then computed as the total amount of usable energy supplied by the turbine per year [34]. The capacity factor (CF) is often thus defined as actual power output divided by the maximum wind power output that can be generated through the system. This wind speed and CF relationship is not continuous, since there is a discontinuous minimum and maximum wind speed required to begin and cease wind power production (the latter to avoid damage

to the wind turbine under extreme wind conditions), and this is represented with different power curves associated with each of the wind farm sites. For this study, the calculated CF at each wind farm site is based on different characteristic power curves specific to each site (see the data in brief accompanying this paper), and do not include electrical losses during the power generation process.

3.2. 80 m wind speed climatology

The remainder of the text focuses on the NC domain and SC domains. Fig. 4 depicts the 80 m wind speed fields (vertically interpolated values except for Virtual Met) from each of the datasets in the NC domain. Wind fields shown are seasonal mean values for all March–April–May (MAM), June–July–August (JJA), September–October–November (SON), December–January–February (DJF) seasons between historical time period 1980–2000. Because of Virtual Met's high spatial resolution (4 km), more topographic features are

apparent in the wind field, whereas the MERRA-2, CFSR, and NARR wind fields are blockier due to their relatively coarse resolution. Comparing VR-CESM to Virtual Met, the overall pattern is very similar, although VR-CESM exhibits lower mean wind speeds overall. This difference will be further assessed as part of the wind farm site comparisons in section 3.2. Fig. 5 depicts mean winds for the SC domain. Again, the patterns remain similar between VR-CESM and Virtual Met, but with a reduced wind magnitude.

Quantitatively, the VR-CESM and Virtual Met product outputs are highly correlated (~0.69), which suggests that the underlying physical mechanisms responsible for determining wind speed are similar between these two products. The slow wind speeds in VR-CESM are likely a consequence of excessive diffusion in the lowest model levels, and further hypothesized to be connected to a boundary layer parameterization in CESM that is not tuned for the high resolutions employed in this study (we anticipate addressing this issue in future work). To better match the wind speeds

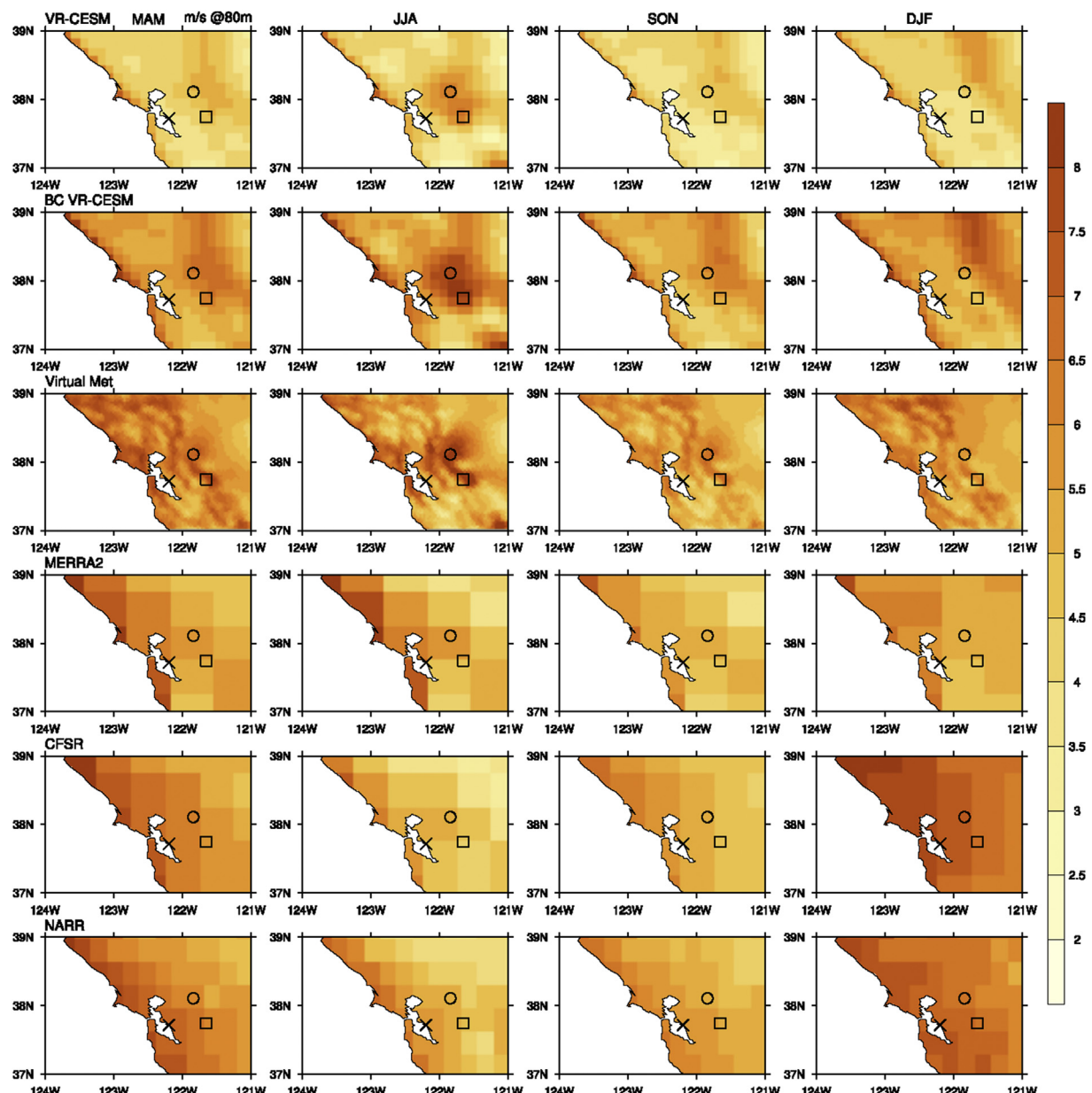


Fig. 4. Seasonal average of interpolated 80 m wind speed from each datasets for historical time period 1980–2000 in northern California domain.

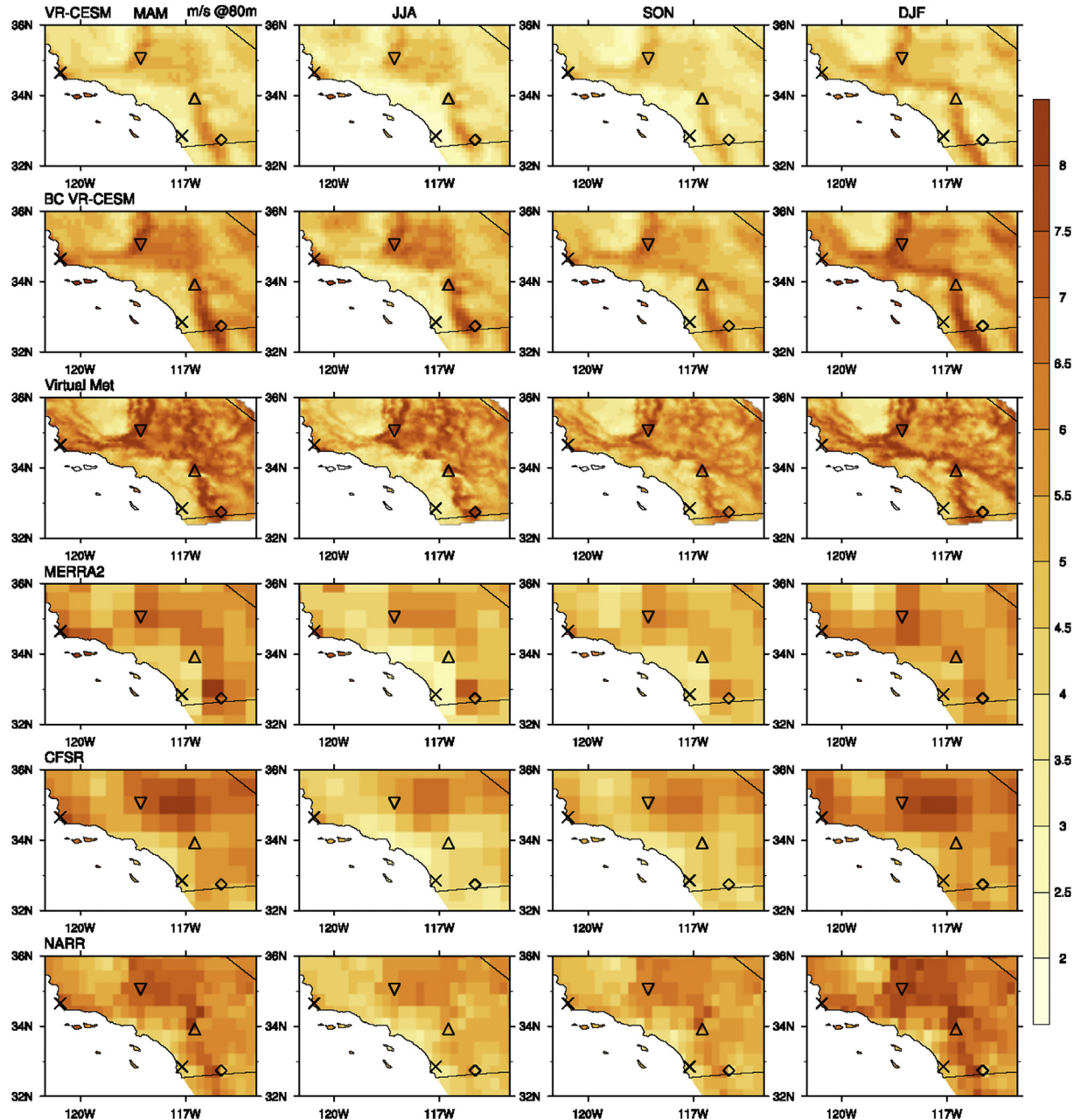


Fig. 5. Seasonal average of interpolated 80 m wind speed from each datasets for historical time period 1980–2000 in southern California domain.

predicted in the virtual met product, we applied a multiplier of 1.30 to the VR-CESM results to produce a bias-corrected VR-CESM (BC VR-CESM) prediction. The value of this multiplier is determined by the mean wind speed difference between VR-CESM and the Virtual Met. As can be seen in Figs. 4 and 5, the wind magnitudes are more comparable to Virtual Met, the latter still produces more spatial variation as compared to BC VR-CESM. This difference in spatial variation can be attributed to the representation of topography in the model – as apparent in Fig. 3, Virtual Met captures the rough rolling terrain of this region, whereas VR-CESM represents the coastal ranges as a single “mound.” As a result, Virtual Met captures a detailed pattern of wind speed variation, whereas VR-CESM only captures a large-scale downslope winds off of this range. In Fig. 8 we observe that the histograms of wind speed from BC VR-CESM are closer to WRF 20 km, although the further downsampled Virtual

Met results exhibit much higher frequencies over the highest wind speed bins at all locations except San Gorgonio. For wind speed fields at the other two analyzed hub heights (50 m and 140 m), please refer to the data in brief. In general, higher altitudes tend to produce larger wind speeds, although the patterns remain quite similar.

Monthly climatological mean wind speeds at each wind farm site are depicted in Fig. 6. As observed in Figs. 4 and 5, Virtual Met tends to produce the highest overall wind speeds. Whereas VR-CESM exhibits a lower wind speed magnitude than Virtual Met, both datasets produce similar spatial patterns that are distinctly different than the other three reanalysis datasets. In particular, the coarser resolution reanalysis data tends to exhibit a weak seasonal cycle. Computing the correlation across monthly mean wind speeds between each dataset with Virtual Met, VR-CESM has the highest

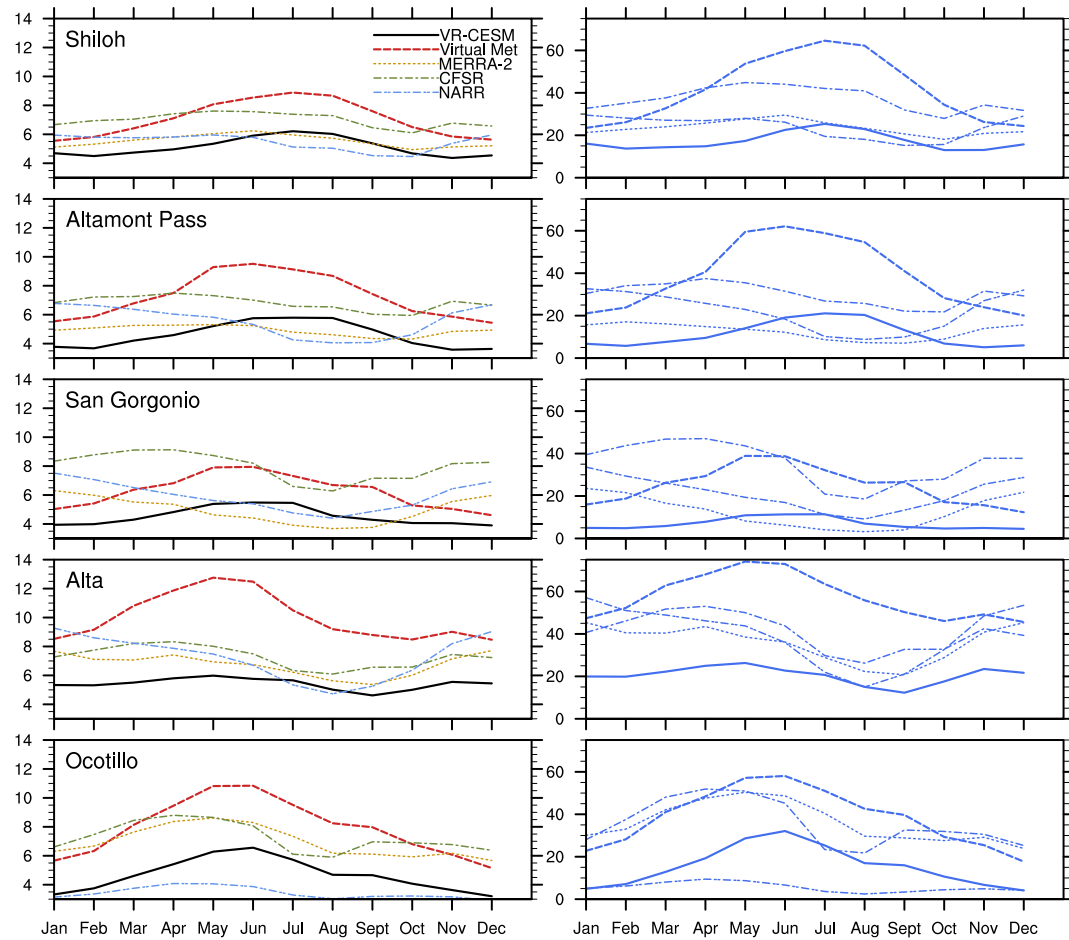


Fig. 6. Monthly mean 80 m wind speed (color-coded lines on left) and mean CF (blue lines on right) at each wind farm site from all datasets during historical time period 1980–2000. (For interpretation of the references to color in this figure legend, the reader is referred to the Web version of this article.)

correlation (on average ~0.87 over all five wind farm sites), followed by MERRA-2 (~0.55), and CFSR (~0.37). NARR (~0.17) exhibited the weakest correlation. To further quantify the spatial correlations between datasets, the centered Pearson pattern correlation (**Table 2**) was calculated for seasonal mean 80 m wind speeds from all the datasets, with the domains masked to only include California, matching the domain from Virtual Met. As observed in **Table 2**, VR-CESM produces the highest pattern correlation (~0.69) with Virtual Met, followed by MERRA-2 (~0.58). Therefore, both temporal and spatial correlation comparisons suggest VR-CESM produces the most similar wind speed climatology (both temporally and spatially) to Virtual Met, followed by MERRA-2. NARR produces the lowest correlation in space and time – in fact, discrepancies in the spatial structure of NARR's wind climatology are likely indicative of potentially significant errors in its representation of wind speeds [David Pierce, personal

communication]. At several sites (particularly San Gorgonio), the seasonality from the three reanalysis datasets is distinctly different from both VR-CESM and Virtual Met. This is again likely a direct result of the resolution discrepancy between the models and reanalysis – for instance, the San Gorgonio wind farm site sits along a narrow pass (~3 km) between mountains, which is not resolved in the reanalysis datasets.

The frequencies of instantaneous 80 m wind speeds from each dataset in **Fig. 7**. Wind speeds in almost all locations appear to follow a Weibull distribution, as is typical for wind speeds where the velocity in each coordinate direction is normally distributed [5,35]. However, the Virtual Met data diverges from the Weibull distribution at several locations, which may be indicative of physical processes that are uniquely captured by this product at high spatial resolution. Specifically, Virtual Met produces higher wind speeds at a higher frequency than other datasets in many cases, leading to a greater spread among the wind speed bins. Frequencies from BC VR-CESM are closer to Virtual Met compared to VR-CESM due to increased wind speed, although there remains a mismatch in the shape of the distribution. The behavior of the Virtual Met data might be related to the analogous method used on WRF model, and further investigation is needed to analyze its impact on the hub-height wind speed. Unfortunately, the authors are presently unaware of any publicly available hub-height wind speed datasets that would allow direct validation of these results against observations.

Table 2

Averaged Pearson pattern correlations between each pair of datasets as obtained from the seasonal mean 80 m wind speed from 1980 to 2000.

Model name	VR-CESM	Virtual Met	MERRA-2	CFSR	NARR
VR-CESM					
Virtual Met	0.69				
MERRA-2	0.61	0.58			
CFSR	0.45	0.53	0.58		
NARR	0.45	0.52	0.51	0.77	
Model name	VR-CESM	Virtual Met	MERRA-2	CFSR	NARR

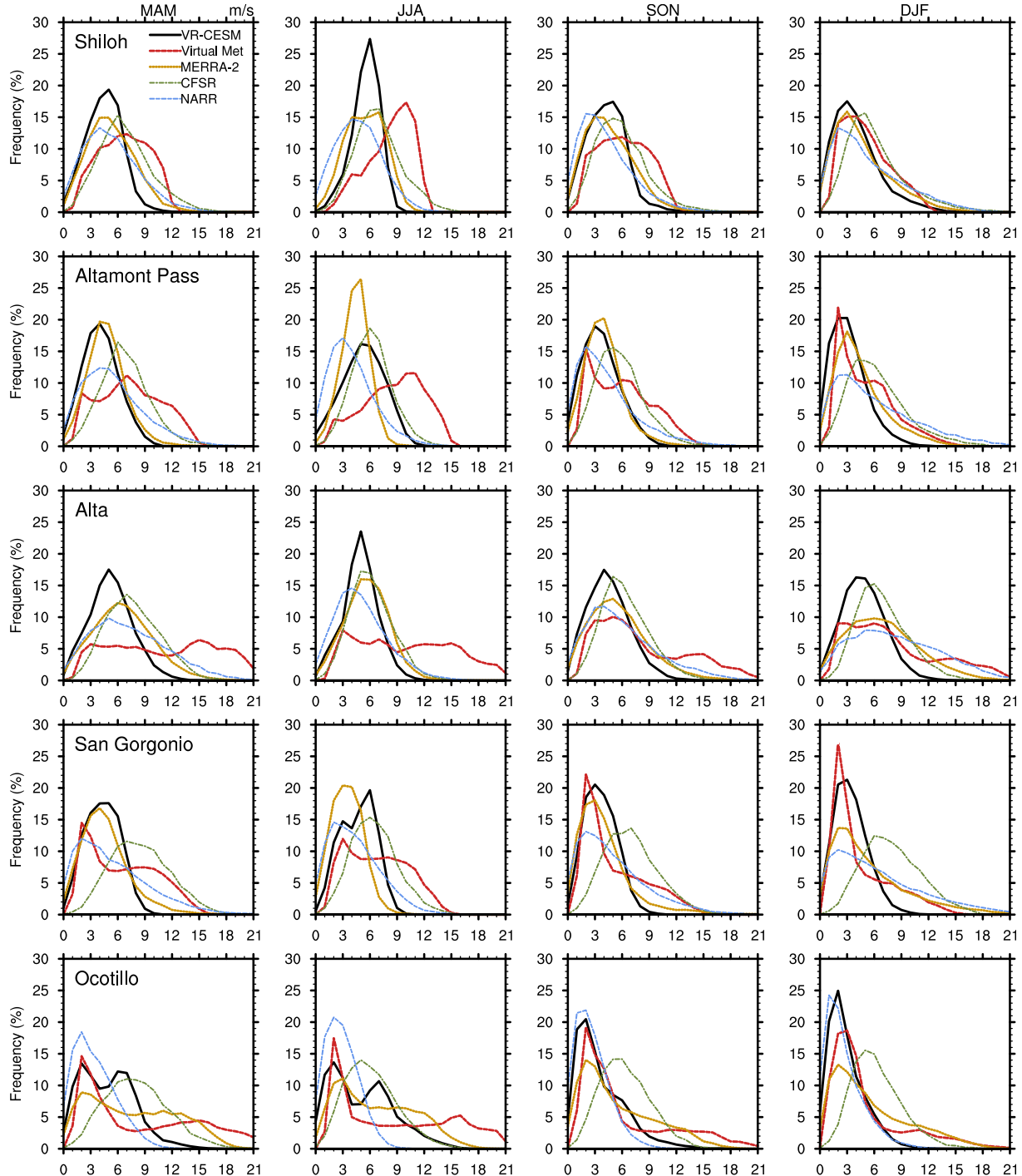


Fig. 7. Frequencies for instantaneous 80 m wind speeds from all datasets at each wind farm location for the historical time period 1980–2000 by season. The bin width is 1 m/s and covers the range from 0 m/s to 21 m/s.

3.3. 10 m wind speed climatology

The performance of VR-CESM is now assessed against the 10 m hourly Integrated Surface Database (ISD). Although ISD incorporates hundreds of observation stations across California, many of these stations do not provide consistent observations over the relevant historical time period (1980–2000). In order to maximize the number of available stations each year, and ensure each year has complete data coverage, validation metrics (Table 3) were calculated separately for each year between 1980

and 2000. Also, to avoid issues with near-surface coastal flow, only inland observation stations were selected for comparison. After imposing these restrictions, an average of 100 inland stations were used from each year.

Table 3 provides the averaged seasonal bias and root-mean-square error (RMSE) at 10 m altitude from our five datasets against ISD observations from 1980 to 2000. Here, a negative (positive) bias indicates that the wind speed is lower (higher) than observations. As observed previously, VR-CESM tends to produce lower wind speeds than observation, whereas the Virtual Met

produces overall higher wind speeds. MERRA-2 and Virtual Met exhibit similar differences, as MERRA-2 provides the boundary conditions for the WRF model; nonetheless, Virtual Met does produce higher mean wind speeds than MERRA-2, likely due to a positive wind bias that appears fairly consistently in the WRF model [36,37]. Note that the values listed for Virtual Met in Table 3 are dependent upon the specific WRF model configuration and initialization used in Virtual Met. Further investigation is required to understand biases in the WRF model. CFSR exhibits lower wind speeds for most of the year except the DJF season, whereas NARR

produces higher wind speeds in all seasons. For MAM and JJA seasons, Virtual Met is very close to observations – namely, it shows a relatively small bias, whereas VR-CESM has strong negative biases in both seasons. In SON and DJF seasons, VR-CESM is closer to observations compared to Virtual Met, particularly during the DJF season (and closer to observations than all other datasets). As VR-CESM also obtains 10 m wind using the lowest model level wind plus similarity theory, the biases in 10 m wind have the potential to be conveyed to higher elevations during the calculation. So this 10 m wind speed comparison with observation

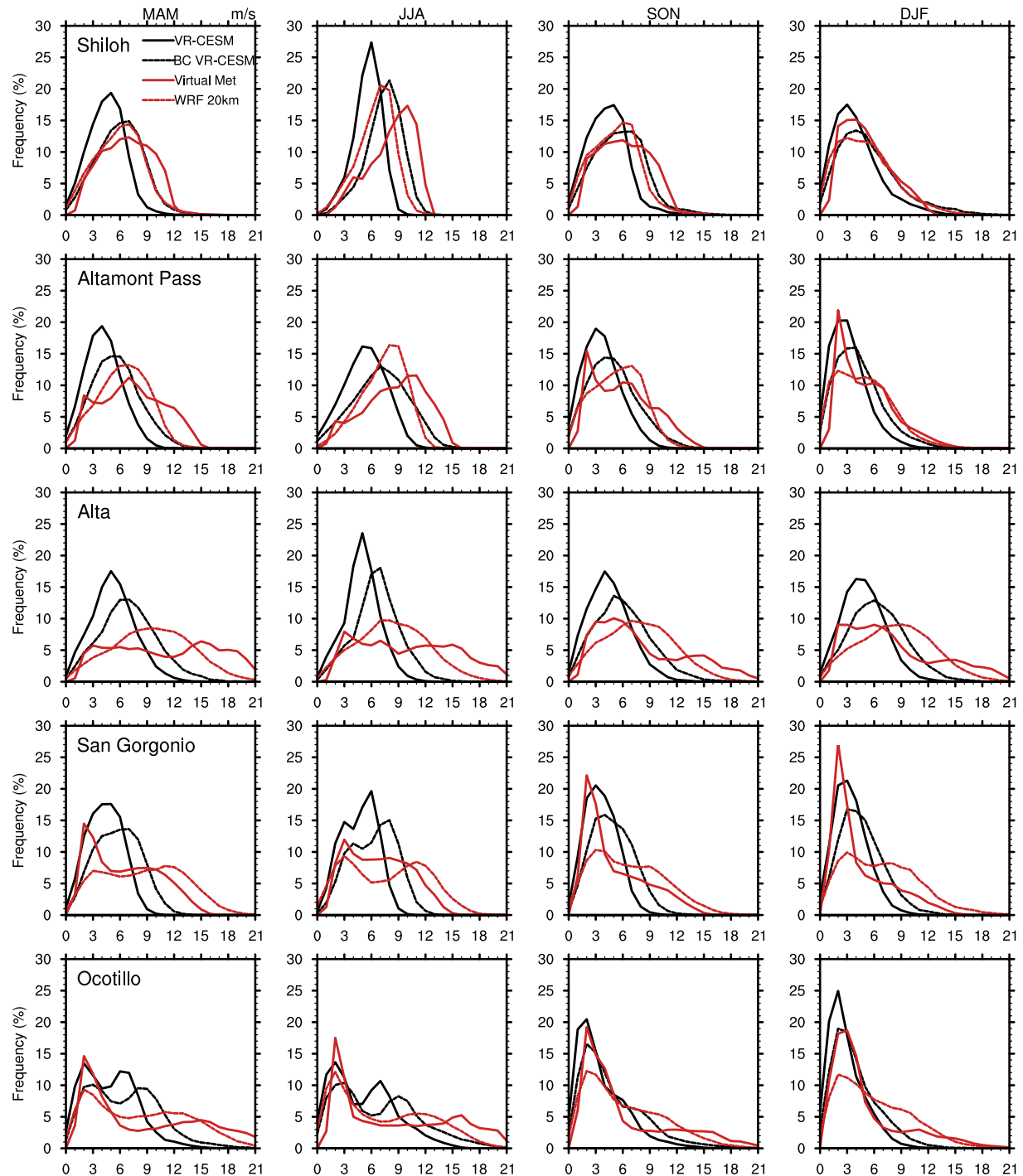


Fig. 8. Frequencies for instantaneous 80 m wind speed from bias-corrected VR-CESM (BC VR-CESM) and 20 km WRF compared to VR-CESM and Virtual Met at each wind farm location for the historical time period 1980–2000. The bin width is 1 m/s and covers the range from 0 m/s to 21 m/s.

Table 3

Bias and RMSE for 10 m wind speed from all five datasets to inland ISD observational stations from 1980 to 2000. Bias and RMSE both have units of m/s.

Model name	Stats	MAM	JJA	SON	DJF	Annual average bias
VR-CESM	Bias	-0.80	-0.52	-0.32	-0.16	-0.45
	RMSE	1.23	1.06	0.88	0.85	
BC VR-CESM	Bias	-0.04	0.21	0.28	0.52	0.24
	RMSE	1.10	1.10	1.00	1.17	
Virtual Met	Bias	0.02	-0.03	0.40	0.56	0.24
	RMSE	0.97	1.02	0.94	1.02	
MERRA-2	Bias	-0.14	-0.13	0.23	0.52	0.12
	RMSE	0.87	0.92	0.78	0.91	
CFSR	Bias	-0.48	-0.50	-0.14	0.23	-0.22
	RMSE	1.11	1.11	0.83	0.88	
NARR	Bias	0.11	0.16	0.52	0.67	0.37
	RMSE	1.34	1.17	1.25	1.49	

also provides us some insight into the possible biases for wind speed at 80 m.

3.4. Comparison with soundings

Hub-height wind data in California is often produced through private investment and hence a closely guarded trade secret confidential to project owners. Consequently, for validation of our modeled hub-height wind speed data against observation, our assessment is limited to a select number of vertical sounding sites across California (listed in Section 2) for comparison of higher level wind speeds, and all of the three soundings are located near the coast (denoted by "X" in Fig. 1) with complex local topographies. The coarse resolution of these models requires them to average inland and offshore wind speeds, leading to skewed results. Also, the sounding observations are only measured twice daily. Both these factors take into account when doing interpolation to calculate 80 m wind from sounding observations, and from model and reanalysis dataset at these sounding locations. In comparison, the three lower resolutions reanalysis datasets all project higher than observation wind speeds. At the OAK site, wind speed

projected from VR-CESM is the closest (bias = 0.95 m/s) to observations in terms of wind magnitude, though Virtual Met captures monthly variation better (correlation = 0.62). However, at VBG and NKX, none of the model datasets could be said to capture the values and seasonal variation particularly well, even though VR-CESM and Virtual Met are the closest among all.

3.5. Comparison between VR-CESM and Virtual Met

To further investigate the difference in wind field between VR-CESM and Virtual Met, the Virtual Met product was regridded to the VR-CESM grid and the difference taken. Fig. 9 shows 1980–2000 seasonally mean wind speed difference from Virtual Met minus VR-CESM, with positive values indicates Virtual Met has higher wind speeds than VR-CESM. The difference is not spatially uniform – in particular, when comparing Fig. 9 alongside Fig. 3, Virtual Met projected higher wind speed over higher altitudes, and lower wind speed at lower altitudes. The five wind farm sites all sit at relatively high topography regions, and consequently Virtual Met projects higher values at all five locations from Fig. 9, consistent with Fig. 6.

4. Future projection

We now turn our attention to future projections of wind energy from VR-CESM mid-century simulation under the RCP8.5 "business as usual" scenario. In this section, seasonal wind power changes are first quantified from the mid-century projection, then understood in terms of the synoptic-scale meteorological shifts associated with these changes at each wind farm site.

4.1. Projected changes

Fig. 10 compares the seasonal 80 m wind speed change between mid-century and historical time periods (2030–2050 minus 1980–2000). These results indicate the SON, DJF, and MAM seasons exhibit decreases in wind speed for all seasons across most areas except for parts of the Central Valley (CV). However, JJA winds were

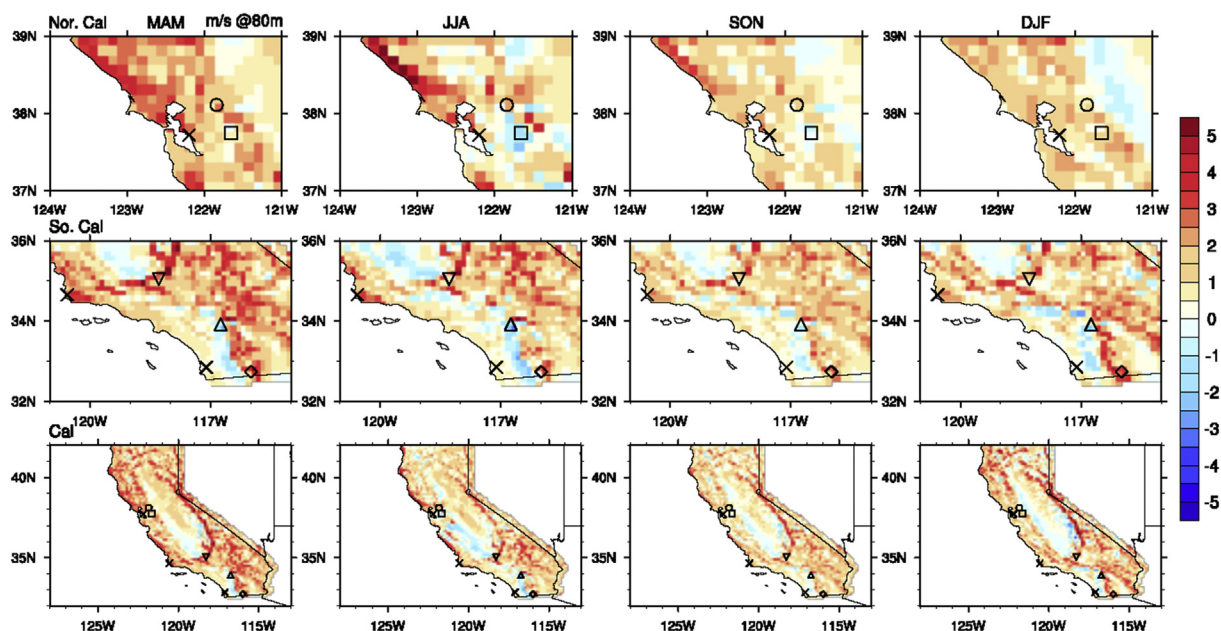


Fig. 9. Comparison between DNV GL Virtual Met 4 km and VR-CESM (Virtual Met minus VR-CESM) of interpolated 80 m wind speed between 1980 and 2000 for northern, southern, and whole states of California domains.

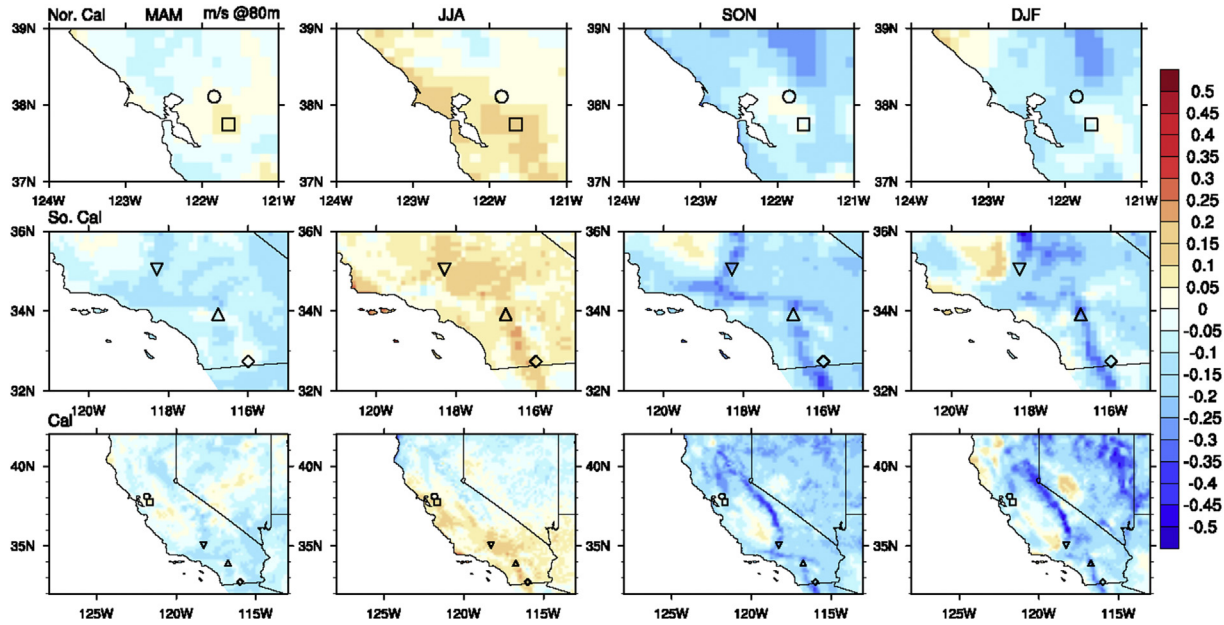


Fig. 10. Comparison of VR-CESM seasonal averaged 80 m wind speed between historical 1980–2000 and mid-century 2030–2050 (mid-century minus historical) for NC, SC, and California domains.

projected to increase in magnitude throughout most of California, particularly through the SC domain.

Comparing historical and future simulations, the seasonal pattern of CF and wind speed at each site was similar, with overall

higher wind speeds during summer months, and lower wind speeds during winter months (Fig. 11). All wind farm sites exhibit a net increase in both wind speed and CF during summer months (JJA), and decrease during winter months (DJF). Annual wind

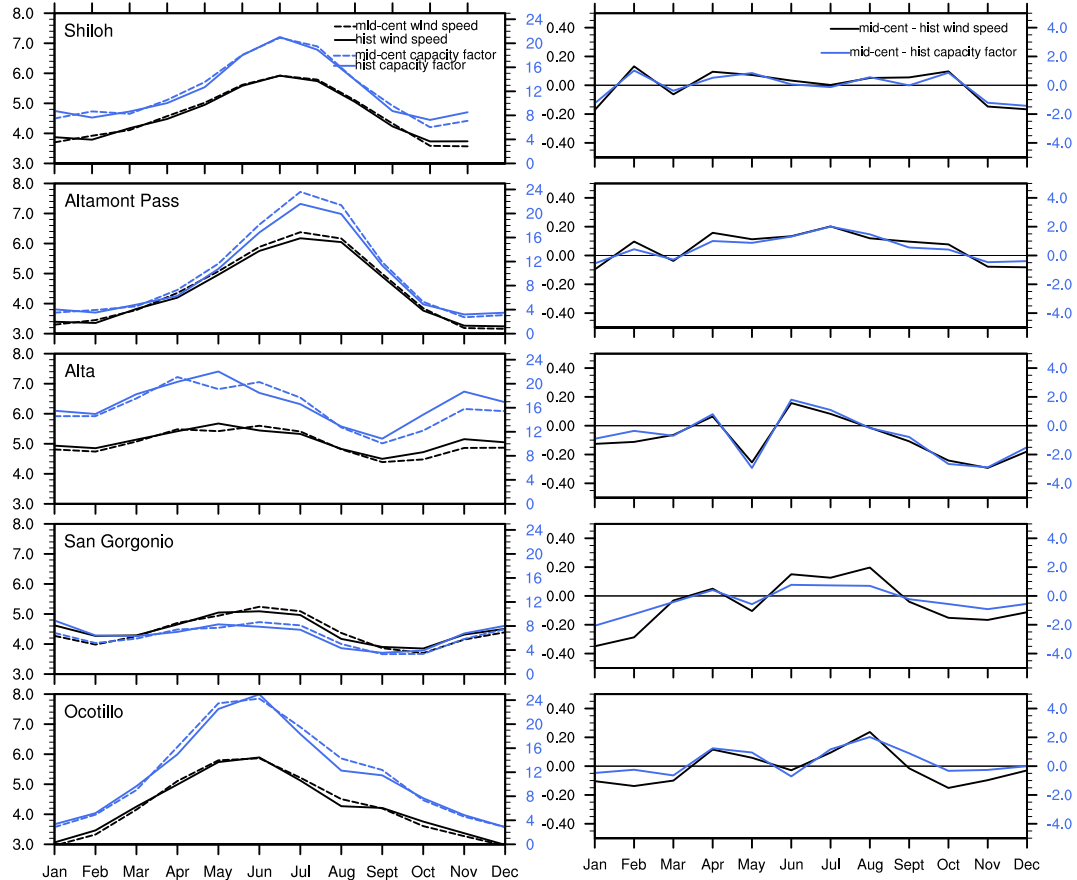


Fig. 11. Comparison of 80 m wind speed and capacity factor between historical and mid-century at each wind farm site.

Table 4

Seasonal and annual capacity factor changes (mid-century CF minus historical CF, divided by historical CF, and written as a percentage) at each wind farm site under mid-century 2030–2050 compared to historical 1980–2000. Boldface indicates a percent change above the 95% significance level.

wind farm	MAM	JJA	SON	DJF	annual
Shiloh	+0.2%	+0.4%	-7.7%	-5.8%	-3.2%
Altamont Pass	+4.2%	+ 7.5%	-4.5%	-0.9%	+1.6%
Alta	-5.1%	+8.3%	- 13.3%	-7.3%	-4.4%
San Gorgonio	-2.4%	+ 9.7%	- 10.9%	- 16.9%	-5.1%
Ocotillo	+1.6%	+5.6%	-2.0%	-9.0%	-1.0%

energy production decreases at all sites except Altamont Pass (Table 4). Consistent with Fig. 11, JJA at all wind farm sites is associated with an increase in CF, while SON and DJF seasons lead to a decrease in CF. The SON CF decrease is consistent with results from Ref. [38], which analyzed possible future trends at the Tehachapi wind farm site (denoted as • in Fig. 1), and projected a significant

decrease in wind speed throughout mid-century Fall months, and little change in Spring-Summer.

An increase in the frequency of lower wind speeds during SON and DJF seasons is indicative of the decreasing trend in wind speed through these two seasons. A decrease in the frequency of lower wind speeds during JJA, and increased frequency of higher wind speeds, is indicative of the increasing trend in wind speed during this season. Fig. 12 depicts the differences in frequency between seasonal 80 m wind speeds over the historical and mid-century periods from VR-CESM. The bold lines in Fig. 12 correspond to the seasons with significant CF changes from Table 4.

4.2. Synoptic-scale drivers

In meteorology, synoptic-scale fields are associated with horizontal scales on the order of 1000 km or more. Mean meteorological fields have been analyzed for seasons with significant CF changes to identify the synoptic-scale drivers that could influence

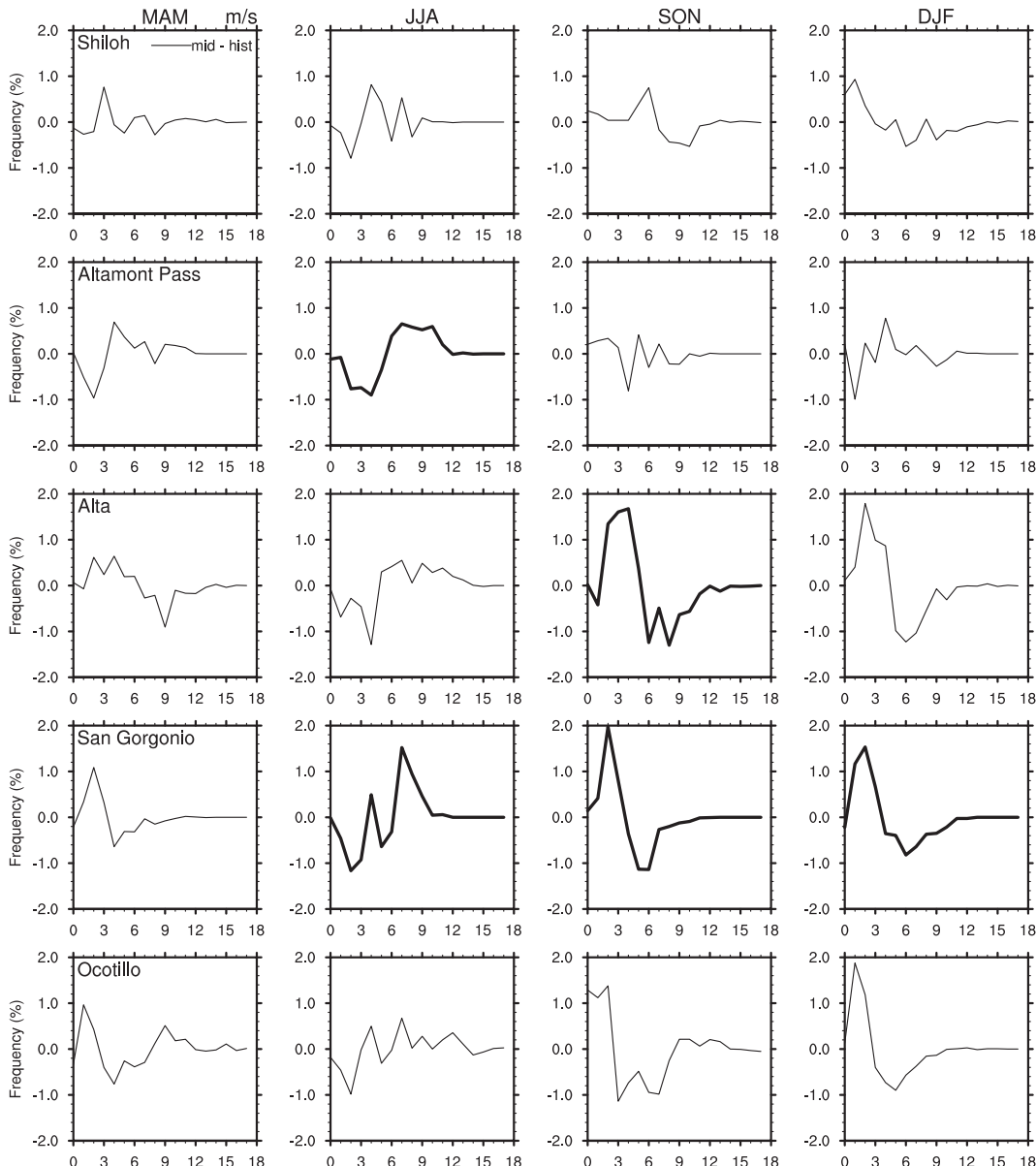


Fig. 12. Differences in frequencies between mid-century 2030–2050 and historical 1980–2000 (mid-century minus historical) for seasonal averaged 80 m wind speed from VR-CESM at each wind farm location. Bold lines correspond to significant changes from Table 4.

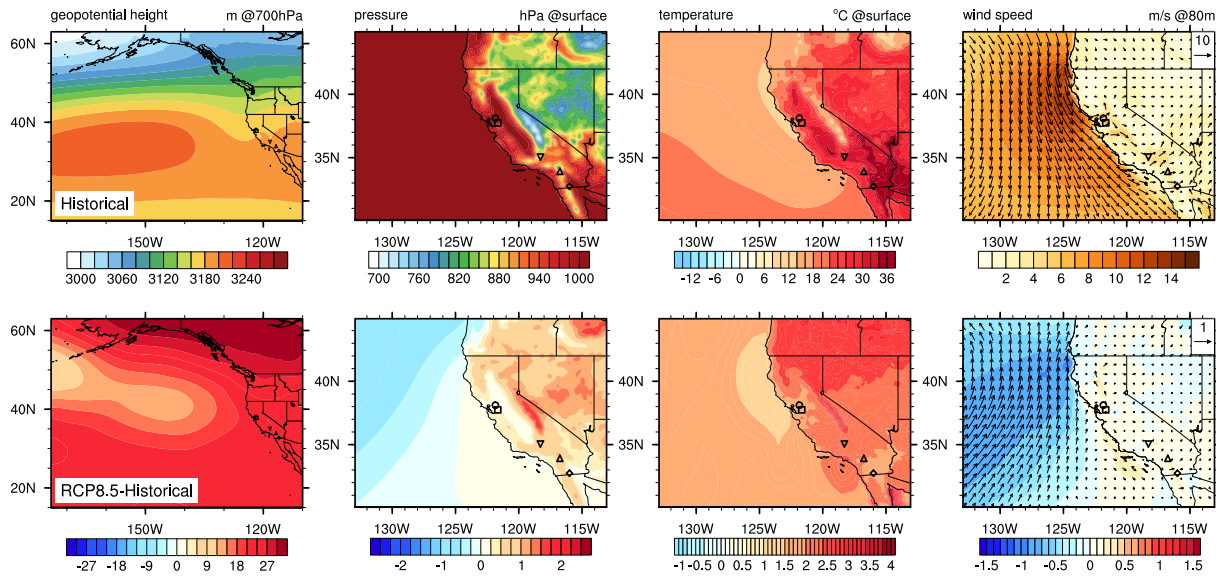


Fig. 13. Seasonal mean 700 hPa geopotential height, surface pressure, surface temperature, and 80 m wind fields on historical 1980–2000 (top row), and the corresponding anomaly fields on mid-century 2030–2050 (bottom row) during JJA season. Anomaly values (bottom row) were calculated from subtracting mean historical fields (top row) from mean mid-century fields.

the historical and mid-century wind climatology (JJA in Fig. 13, SON in Fig. 14, DJF in Fig. 15). In particular, our analysis focuses on the 700 hPa geopotential height field, which is defined as the height of 700 hPa isobar surfaces above mean sea level, as well as surface pressure, surface temperature, and hub height wind speed at 80 m overlaid with wind direction at the same height. The 700 hPa geopotential height field was analyzed as it is reflective of the general circulation, with wind flow at this level largely geostrophic and hence following constant geopotential contours. The surface pressure field also impacts local wind speeds, and is closely associated with surface temperature changes. Synoptic-scale fields during the MAM season were not investigated, as there was no significant CF change detected over this period (see Table 4).

Through JJA (Fig. 13), the 700 hPa geopotential height field features an off-shore trough and geopotential height contour lines perpendicular to coast. This pattern is indicative of a typical summertime marine air penetration condition [39–41] and is driven by the off-shore trough modifying the geopotential height contour lines to be perpendicular to the coastline, allowing cool and moist marine air to penetrate inland. The location of the off-shore trough is directly responsible for driving marine air through the San Francisco Bay Delta. Relative to the historical period, the magnitude of the 700 hPa geopotential height field under the mid-century increases (as a direct consequence of low-level warming). However, this increase is less pronounced over the Northern Pacific, which drives a weakening of the typically northerly wind pattern

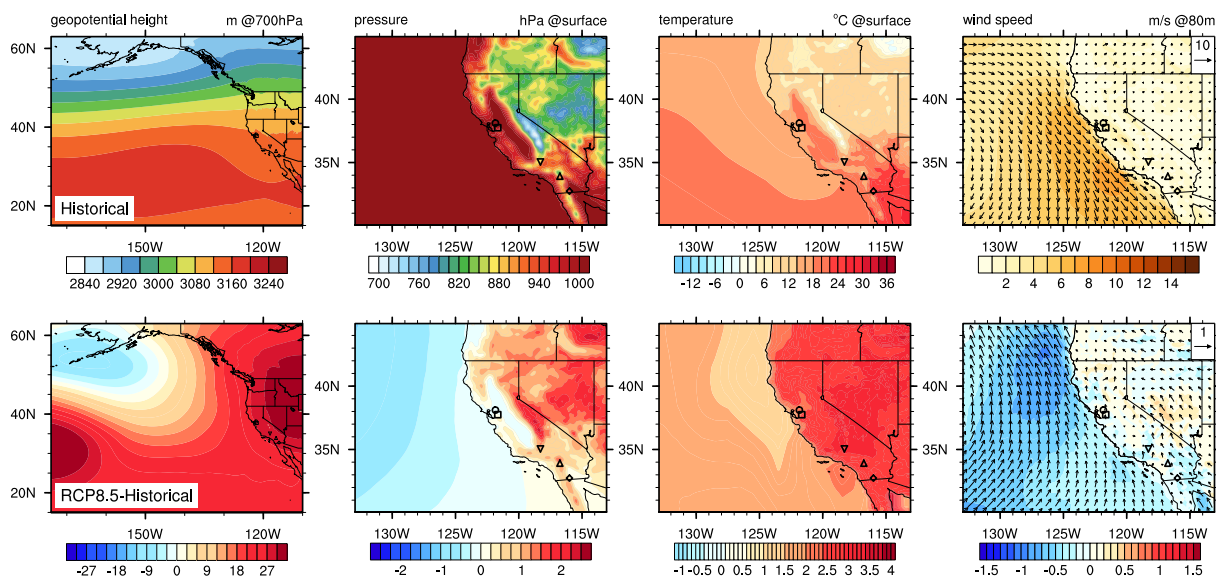


Fig. 14. Seasonal mean 700 hPa geopotential height, surface pressure, surface temperature, and 80 m wind fields on historical 1980–2000 (top row), and the corresponding anomaly fields on mid-century 2030–2050 (bottom row) during SON season.

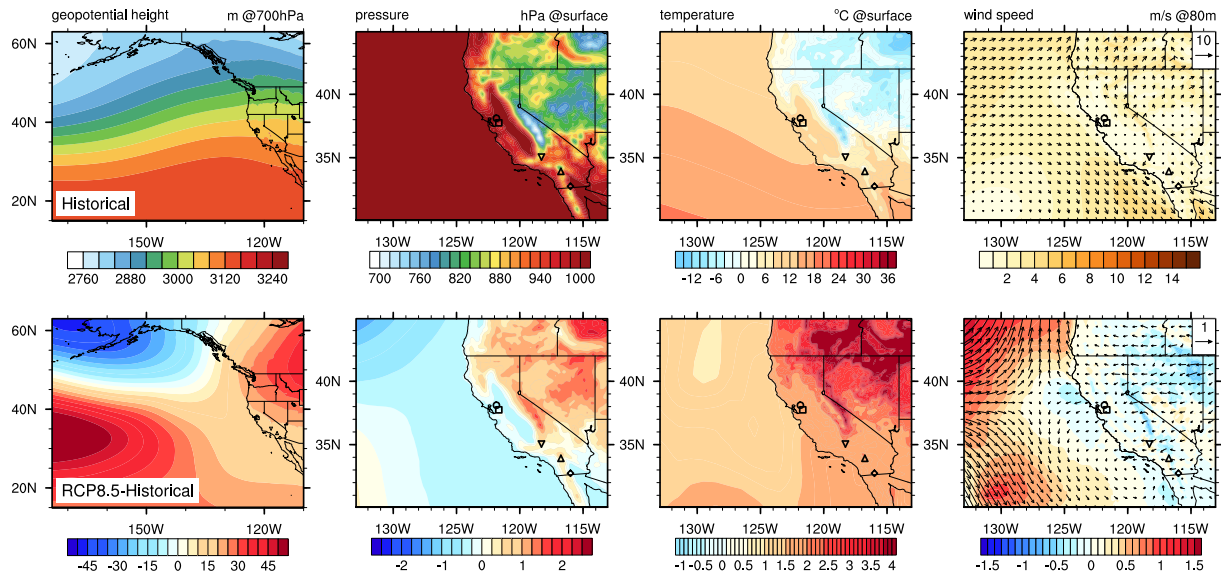


Fig. 15. Seasonal mean 700 hPa geopotential height, surface pressure, surface temperature, and 80 m wind fields on historical 1980–2000 (top row), and the corresponding anomaly fields on mid-century 2030–2050 (bottom row) during DJF season.

that traces the coastline in Northern California, and an increase in the on-shore flow pattern driven by the general circulation. This in turn leads to an increase in wind speeds through the San Francisco Delta region (Shiloh and Altamont Pass in NC domain). A shift in this synoptic-scale pattern also drives increased ventilation in the SC domain.

Surface pressure in JJA is also observed to increase more rapidly at higher altitudes – consequently the surface pressure in the Mojave desert increases more rapidly than the Central Valley, and leads to a weaker pressure gradient between the CV and Mojave. A similar observation was made by Ref. [42] to explain a projected decrease in Santa Ana wind events in this region during the Fall season. Although this is a potential driver for wind speed decrease at Alta in SC, the impact of a reduced pressure gradient is counterbalanced by the changes to the large-scale geopotential height field, which enhances westerly wind throughout California.

Across both time periods, SON wind speeds are generally reduced in comparison to JJA, partly due to the decrease in land-sea temperature contrast, and associated reduction to marine air penetration. Comparing the 700 hPa geopotential height field between historical and mid-century during SON, the entirety of the California coast is under the influence of the weakening of wind flow parallel to the coast, driven by the negative geopotential anomaly south of Alaska, and accompanied by a positive geopotential height anomaly over the continent. Through the SC domain, a weakening pressure gradient drives a decrease in the wind speed at Alta and San Gorgonio. This observation is in agreement with the observations of [38], and leads to a projected 10–15% power potential decrease during Fall season in mid-century.

Through DJF (Fig. 15), increased geopotential height over the sub-tropical western Pacific and the North American continent lead to a weaker northerly flow parallel to the coast and a reduced on-shore flow. Further, with surface pressure decreases in the CV, the surface-level pressure gradient between the CV and the Mojave desert decreases, which would in turn be expected to drive lower wind speeds at the Alta wind farm site. The surface pressure gradient also decreases between the inland and the adjacent ocean near San Gorgonio wind farm site, which further enhances the wind speed decrease.

The seasonal meteorological patterns under the mid-century RCP8.5 scenario provide further evidence that future changes of wind energy in California will be influenced by both the synoptic-scale and local changes. Overall, the synoptic analysis suggests that the climate through mid-century will be conducive to higher wind speed across the whole state of California during JJA (5–10% at four of the five sites examined), and lower during SON (particularly at Alta and San Gorgonio which each exhibited a >10% decrease) and DJF (with a 17% decrease at San Gorgonio). The changes to the surface pressure gradient between the Central Valley and the Mojave Desert appears robust across seasons and is a primary driver of wind speed decreases in the SC domain. To ensure the synoptic-scale climatology of VR-CESM was not an outlier, synoptic-scale geopotential height fields were also examined across CMIP5 models over the same time period and similar trends were observed. Ensemble runs with VR-CESM could potentially add confidence to this study, and are a topic for future exploration once the identified biases in VR-CESM are addressed. Besides the mid-century time frame (2030–2050) that was studied in this paper, another VR-CESM simulation over the end-of-century time frame (2080–2100) was also conducted using the same model configuration. Wind speed change at each wind farm site from the end-of-century run had the same sign as the mid-century run, and relatively greater magnitude. The results from the end-of-century run adds confidence to our current analysis. However, due to the end-of-century time frame is outside the typical lifetime of a wind farm (~20–25 years), the analysis from end-of-century was not included in this paper.

5. Discussion and conclusions

The goal of this paper is twofold: First, to validate and assess the performance of VR-CESM as a tool for modeling near-surface wind speeds and, second, to leverage VR-CESM to assess the drivers of future wind speed change in California. The main conclusions of this paper follow.

The capacity of the VR-CESM variable-resolution global climate modeling system was assessed at correctly representing the historical character of wind field in California (1980–2000) against a high-resolution WRF statistically-downscaled wind data product,

multiple reanalysis products, and publicly available observational data. Our results suggest that although VR-CESM generally exhibited a bias towards slower wind speeds inland, the monthly climatology and spatial pattern associated with the wind field was approximately consistent with observations. Although the wind climatology was greatly improved over coarse resolution reanalysis products, we believe that the local model resolution (14 km) is still too coarse for regions of rapid topographic variation. Nonetheless, rough agreement between simulated and observed wind fields led us to conclude that VR-CESM is correctly representing the key regional and synoptic-scale processes that are relevant for wind speed forecasts. Further work is needed to determine the source of the slow bias in near-surface wind speeds from CESM.

Second, this study aimed to project and understand hub-height wind speed changes at each wind farm site, using a VR-CESM mid-century (2030–2050) simulation under RCP8.5. To better understand the regional and synoptic-scale drivers that are responsible for these changes, our analysis targeted the meteorological patterns associated with large-scale shifts in wind character. The five major wind farm sites considered in this study spanned California. At almost all wind farm sites, significant seasonal changes were observed in the capacity factor, with an increase in summertime (JJA) resources and a decrease in fall (SON) and winter (DJF) under RCP8.5 at all five sites (Table 4). Synoptic-scale and localized drivers behind season wind energy change were also identified, and suggested climate change may favor synoptic patterns that lead to higher wind speed during JJA, and lower wind speed during SON and DJF.

Overall, this study improves the characterization of uncertainty around the magnitude and variability in space and time of Californians wind resources in the near future, and also enhances our understanding of the physical mechanisms related to the trends in wind resource variability.

There are many climatological factors that impact on the wind energy in California, including correlations of wind speed with climate modes such as El Niño–Southern Oscillation (ENSO), Pacific Decadal Oscillation (PDO), and North Atlantic Oscillation (NAO). Because of the long temporal frequency of these climate modes, there is some difficulty in disentangling how these climate modes have historically impacted wind resources. In this context, ensemble simulations with VR-CESM may be valuable at modeling these connections. Future work could also address alternative statistical strategies for identifying change in wind fields: for instance, the use of a clustering method to analyze and group relevant wind patterns in California. Such a method could be used to investigate the potential historical and future trends from different wind patterns. Possible future study will also focus on analyzing the capacity of models to capture, and the climate change impact on intense and extreme winds.

Acknowledgment

The authors want to thank the Craig Collier, Daran Rife, and Christopher Hayes for the helpful conversations throughout this project. We would further like to thank the two anonymous reviewers for their thorough evaluation of the manuscript and suggested improvements. Funding for this work comes from the California Energy Commission EPIC program under award EPC-15-068. This project is further supported by the National Institute of Food and Agriculture, U.S. Department of Agriculture, hatch project under California Agricultural Experiment Station project CA-D-LAW-2203-H. Author Ullrich is supported by Department of Energy Office of Science award number DE-SC0016605, “An Integrated Evaluation of the Simulated Hydroclimate System of the Continental US”.

References

- [1] O. Edenhofer, R. Pichs-Madruga, Y. Sokona, K. Seyboth, S. Kadner, T. Zwickel, P. Eickemeier, G. Hansen, S. Schlömer, C. von Stechow, et al., *Renewable Energy Sources and Climate Change Mitigation: Special Report of the Intergovernmental Panel on Climate Change*, Cambridge University Press, 2011.
- [2] R. Barthelmie, S. Pryor, Potential contribution of wind energy to climate change mitigation, *Nat. Clim. Change* 4 (8) (2014) 684–688.
- [3] R. Vautard, J. Cattiaux, P. Yiou, J.-N. Thépaut, P. Ciais, Northern hemisphere atmospheric stilling partly attributed to an increase in surface roughness, *Nat. Geosci.* 3 (11) (2010) 756.
- [4] S. Pryor, R.J. Barthelmie, J. Schoof, Inter-annual variability of wind indices across europe, *Wind Energy* 9 (1–2) (2006) 27–38.
- [5] S. Pryor, R. Barthelmie, Climate change impacts on wind energy: a review, *Renew. Sustain. Energy Rev.* 14 (1) (2010) 430–437.
- [6] M.K. Hubbert, Energy resources of the Earth, *Sci. Am.* 224(3).
- [7] D. Rasmussen, T. Holloway, G. Nemet, Opportunities and challenges in assessing climate change impacts on wind energy – a critical comparison of wind speed projections in California, *Environ. Res. Lett.* 6 (2) (2011) 024008.
- [8] L. Yu, S. Zhong, X. Bian, W.E. Heilman, Temporal and spatial variability of wind resources in the United States as derived from the Climate Forecast System Reanalysis, *J. Clim.* 28 (3) (2015) 1166–1183.
- [9] S. Pryor, R. Barthelmie, Assessing climate change impacts on the near-term stability of the wind energy resource over the United States, *Proc. Natl. Acad. Sci. Unit. States Am.* 108 (20) (2011) 8167–8171.
- [10] D.J. Sailor, M. Smith, M. Hart, Climate change implications for wind power resources in the Northwest United States, *Renew. Energy* 33 (11) (2008) 2393–2406.
- [11] S. Pryor, R. Barthelmie, E. Kjellström, Potential climate change impact on wind energy resources in northern Europe: analyses using a regional climate model, *Clim. Dynam.* 25 (7–8) (2005) 815–835.
- [12] C.L. Archer, M.Z. Jacobson, Spatial and temporal distributions of US winds and wind power at 80 m derived from measurements, *J. Geophys. Res.: Atmosphere* 108 (D9) (2003).
- [13] M. Segal, Z. Pan, R.W. Arritt, E.S. Takle, On the potential change in wind power over the US due to increases of atmospheric greenhouse gases, *Renew. Energy* 24 (2) (2001) 235–243.
- [14] A.M. Rhoades, X. Huang, P.A. Ullrich, C.M. Zarzycki, Characterizing Sierra Nevada snowpack using variable-resolution CESM, *J. Appl. Meteorol. Climatol.* 55 (1) (2016) 173–196.
- [15] X. Huang, A.M. Rhoades, P.A. Ullrich, C.M. Zarzycki, An evaluation of the variable-resolution CESM for modeling California's climate, *J. Adv. Model. Earth Syst.* 8 (1) (2016) 345–369.
- [16] A.M. Rhoades, P.A. Ullrich, C.M. Zarzycki, Projecting 21st century snowpack trends in western USA mountains using variable-resolution CESM, *Clim. Dynam.* (2017) 1–28.
- [17] X. Huang, P.A. Ullrich, Irrigation impacts on California's climate with the variable-resolution CESM, *J. Adv. Model. Earth Syst.* 8 (3) (2016) 1151–1163.
- [18] C.M. Zarzycki, C. Jablonowski, D.R. Thatcher, M.A. Taylor, Effects of localized grid refinement on the general circulation and climatology in the Community Atmosphere Model, *J. Clim.* 28 (7) (2015) 2777–2803.
- [19] R.B. Neale, C.-C. Chen, A. Gettelman, P.H. Lauritzen, S. Park, D.L. Williamson, A.J. Conley, R. Garcia, D. Kinnison, J.-F. Lamarque, et al., Description of the NCAR Community Atmosphere Model (CAM 5.0), NCAR Tech. Note NCAR/TN-486+STR.
- [20] J.M. Dennis, J. Edwards, K.J. Evans, O. Guba, P.H. Lauritzen, A.A. Mirin, A. St-Cyr, M.A. Taylor, P.H. Worley, CAM-SE: a scalable spectral element dynamical core for the Community Atmosphere Model, *Int. J. High Perform. Comput. Appl.* 26 (1) (2012) 74–89.
- [21] C.M. Zarzycki, M.N. Levy, C. Jablonowski, J.R. Overfelt, M.A. Taylor, P.A. Ullrich, Aquaplanet experiments using CAMs variable-resolution dynamical core, *J. Clim.* 27 (14) (2014) 5481–5503.
- [22] P.A. Ullrich, SQuadGen: Spherical Quadrilateral Grid Generator, University of California, Davis, Climate and Global Change Group Software, 2014. Available online at: <http://climate.ucdavis.edu/squadgen.php>.
- [23] O. Guba, M.A. Taylor, P.A. Ullrich, J.R. Overfelt, M.N. Levy, The spectral element method on variable resolution grids: evaluating grid sensitivity and resolution-aware numerical viscosity, *Geosci. Model Dev. Discuss.* 7 (2014) 4081–4117.
- [24] K.E. Taylor, R.J. Stouffer, G.A. Meehl, An overview of CMIP5 and the experiment design, *Bull. Am. Meteorol. Soc.* 93 (4) (2012) 485.
- [25] L. Delle Monache, F.A. Eckel, D.L. Rife, B. Nagarajan, K. Searight, Probabilistic weather prediction with an analog ensemble, *Mon. Weather Rev.* 141 (10) (2013) 3498–3516.
- [26] L. Delle Monache, T. Nipen, Y. Liu, G. Roux, R. Stull, Kalman filter and analog schemes to postprocess numerical weather predictions, *Mon. Weather Rev.* 139 (11) (2011) 3554–3570.
- [27] R. Gelaro, W. McCarty, M.J. Suárez, R. Todling, A. Molod, L. Takacs, C.A. Randles, A. Darmenov, M.G. Bosilovich, R. Reichle, et al., The modern-era retrospective analysis for research and applications, version 2 (MERRA-2), *J. Clim.* 30 (14) (2017) 5419–5454.
- [28] M.M. Rienecker, M.J. Suarez, R. Gelaro, R. Todling, J. Bacmeister, E. Liu, M.G. Bosilovich, S.D. Schubert, L. Takacs, G.-K. Kim, et al., MERRA: NASA's modern-era retrospective analysis for research and applications, *J. Clim.* 24

- (14) (2011) 3624–3648.
- [29] Goddard Earth Sciences Data and Information Services Center (GES DISC), MERRA-2_inst3_3d_asm_Np: 3d,3-Hourly,Instantaneous,Pressure-Level,Assimilation,Assimilated Meteorological Fields V5.12.4 <https://doi.org/10.5067/QBZ6MG944HWO>.
- [30] Goddard earth sciences data and information services center (ges disc), merra-2_inst1_2d_asm_Nx: 2d,1-hourly,instantaneous,single-level,assimilation,single-level diagnostics v5.12.4 <https://doi.org/10.5067/3Z173KIE2TPD>.
- [31] S. Saha, S. Moorthi, H. Pan, X. Wu, J. Wang, S. Nadiga, P. Tripp, R. Kistler, J. Woollen, D. Behringer, et al., NCEP Climate Forecast System Reanalysis (CFSR) 6-hourly Products, January 1979 to December 2010, Research Data, The National Center for Atmospheric Research, Computational and Information Systems Laboratory, Boulder, Colo, USA.
- [32] F. Mesinger, G. DiMego, E. Kalnay, K. Mitchell, P.C. Shafran, W. Ebisuzaki, D. Jović, J. Woollen, E. Rogers, E.H. Berbery, et al., North American regional reanalysis, *Bull. Am. Meteorol. Soc.* 87 (3) (2006) 343–360.
- [33] C. Justus, A. Mikhail, Height variation of wind speed and wind distributions statistics, *Geophys. Res. Lett.* 3 (5) (1976) 261–264.
- [34] M. Fripp, R.H. Wiser, Effects of temporal wind patterns on the value of wind-generated electricity in California and the Northwest, *IEEE Trans. Power Syst.* 23 (2) (2008) 477–485.
- [35] S.E. Tuller, A.C. Brett, The goodness of fit of the weibull and Rayleigh distributions to the distributions of observed wind speeds in a topographically diverse area, *Int. J. Climatol.* 5 (1) (1985) 79–94.
- [36] S. Shimada, T. Ohsawa, S. Chikaoka, K. Kozai, Accuracy of the wind speed profile in the lower PBL as simulated by the WRF model, *Sola* 7 (2011) 109–112.
- [37] D. Carvalho, A. Rocha, M. Gómez-Gesteira, C.S. Santos, WRF wind simulation and wind energy production estimates forced by different reanalyses: comparison with observed data for Portugal, *Appl. Energy* 117 (2014) 116–126.
- [38] P.B. Duffy, J. Bartlett, J. Dracup, J. Freedman, K. Madani, K. Waight, Climate Change Impacts on Generation of Wind, Solar, and Hydropower in California, California Energy Commission, 2014. CEC5002014111.
- [39] M. Wang, P. Ullrich, Marine air penetration in California's central valley: meteorological drivers and the impact of climate change, *J. Appl. Meteorol. Climatol.* 57 (1) (2018) 137–154.
- [40] S. Beaver, A. Palazoglu, Cluster analysis of hourly wind measurements to reveal synoptic regimes affecting air quality, *J. Appl. Meteorol. Climatol.* 45 (12) (2006) 1710–1726.
- [41] M.A. Fosberg, M.J. Schroeder, Marine air penetration in central California, *J. Appl. Meteorol.* 5 (5) (1966) 573–589.
- [42] N.L. Miller, N.J. Schlegel, Climate change projected fire weather sensitivity: California Santa Ana wind occurrence, *Geophys. Res. Lett.* 33(15).